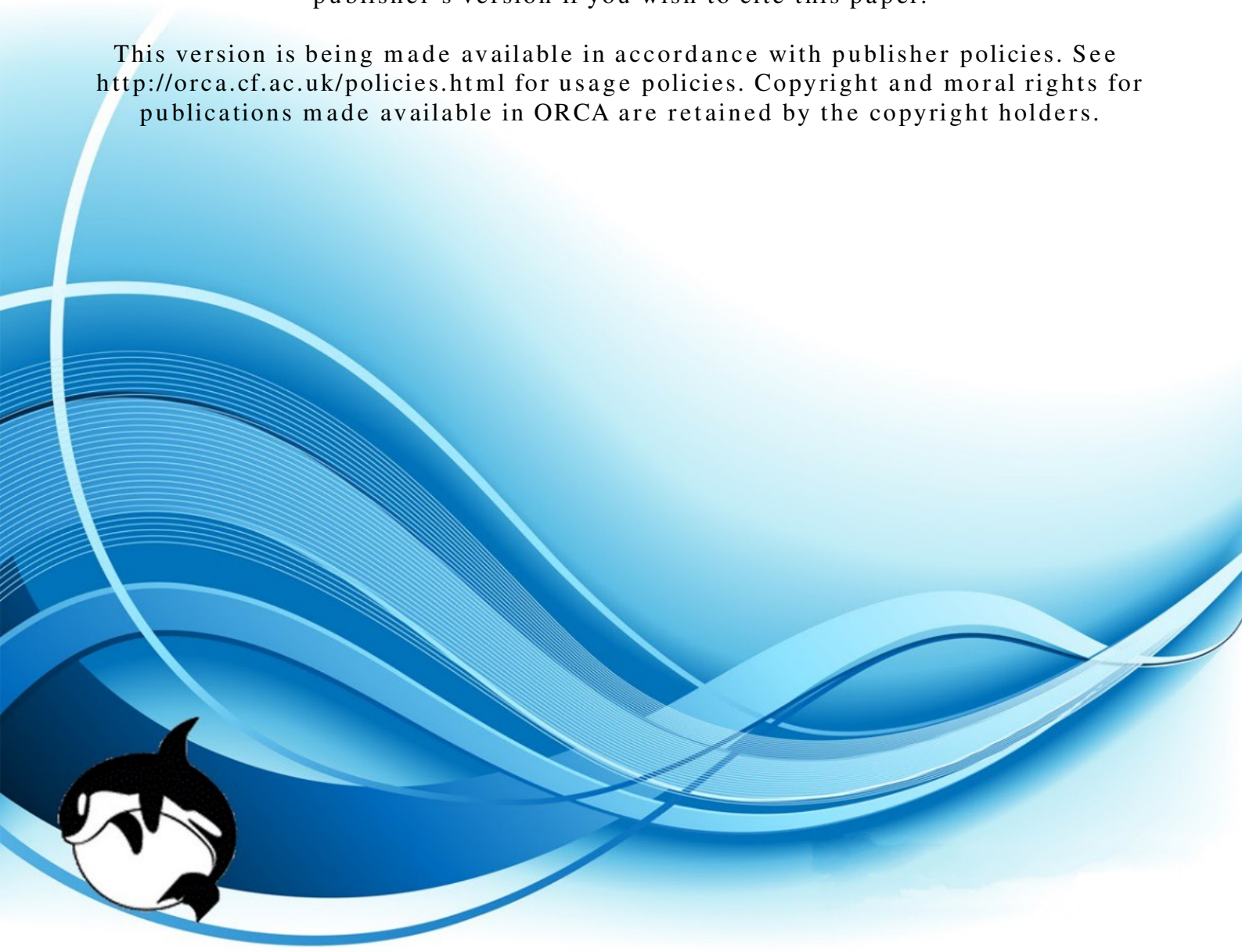

Discrete element simulation of powder layer thickness in laser additive manufacturing

Quanqan Han*, Heng Gu, Rossi Setchi*,

[a]Cardiff School of Engineering, Cardiff University, Cardiff, CF24 3AA, UK

Corresponding author: Quanquan Han: Hanq1@cardiff.ac.uk, +4402920876266

Rossi Setchi: Setchi@cardiff.ac.uk, +4402920875720

Abstract

The optimisation of the laser additive manufacturing (AM) process is a challenging task when a new material is considered. Compared to the selection of other process parameters such as laser power, scanning speed and hatch spacing, optimisation of powder layer thickness is much more time-consuming and costly because a new run is normally needed when the layer thickness value is changed. In practice, the layer thickness is fixed to a value that is slightly higher than the average particle size. This paper introduces a systematic approach to layer thickness optimisation based on a theoretical model of the interactions between the particles, the wiper and the build plate during the powder deposition. The focus is on a systematic theoretical and experimental investigation of the effect of powder layer thickness on various powder bed characteristics during single-layer and multi-layer powder deposition. The theoretical model was tested experimentally using Hastelloy X (HX) with an average particle size of 34.4 µm. The experimental results validated the simulation model, which predicted a uniform powder bed deposition when employing a 40 µm layer thickness value. Lower (30 µm) and higher (50 µm) layer thickness values resulted in large voids and short-feed defects, respectively. The subsequent optimisation of the scanning speed and hatch spacing parameters was executed using a 40 µm layer thickness. The optimum process parameters were then used to examine the microstructure and tensile performance of the as-fabricated HX. This study provides an improved understanding of the powder deposition process and offers insights into the selection of suitable powder layer thicknesses in laser AM.

Keywords: Layer thickness; powder deposition; laser additive manufacturing; Hastelloy X; discrete element method; microstructure

1. Introduction

Laser additive manufacturing (AM) is an established technology for the direct fabrication of metal components with complex geometries using layer-by-layer powder deposition and a high-power laser [1] [2] [3]. A wide range of metallic materials can be successfully processed using laser AM, including steel [4], titanium [5] [6], aluminium [7][8][9], nickel [10][11] and various composites. A variety of powder bed characteristics are critical to achieving a quality process because they affect the dimensional accuracy and structural integrity of the fabricated parts.

Several factors, including particle size distribution, layer thickness, recoating speed and blade type, influence the powder bed characteristics in AM. For example, Sutton et al. [12], who reviewed various powder characterisation techniques and the effects of powder characteristics on part properties in powder bed fusion processes, highlighted particle morphology, chemistry and microstructure. Haeri [13] used the discrete element method (DEM) to investigate blade-type spreaders; the author found that an optimised blade profile using sphere approximation was capable of producing a bed with qualities comparable to one created by a roller. The particle-based simulation model developed by Parteli et al. [14] showed that increases in the recoating speed and broader size distributions of the particles, contributed to higher surface roughness of the powder bed. This finding was confirmed by Haeri et al. [15], who used DEM to investigate the effects of particle shape and operating conditions on powder bed surface roughness and solid volume fraction. A roller-type spreader was found to have resulted in better deposition behaviour compared to a blade-type spreader. Some studies have investigated the particle adhesion and the coating process in laser AM [16] [17]. For instance, Meier et al. proposed an adhesion force law, which was capable of predicting the effective surface energy of metal powders [18]. A numerical study was performed to simulate how powder was transferred from the source to the processing table, in which a parameter study was conducted to identify the influence of process table displacement and wiper speed on the powder distribution [19].

Other studies have focussed on the interactions that occur during the material deposition process. Lee et al. [20], who used a DEM model to study the mechanical contact forces and moments between individual particles within the laser AM powder

packing process, found that mass scaling (i.e. the particle density was amplified) is an efficient method for speeding computations. The calculated packing density was not found to be sensitive to the key simulation parameters, such as the inter-particle friction coefficient and the damping coefficient. Markl et al. [21] proposed a DEM-based powder layer deposition algorithm for AM simulations that includes a coupling to a grid-based solver and a choice of parameters. The algorithm the authors developed was capable of producing powder layers with a physical relative density and powder particle size distribution suitable for laser AM. Foroozmehr et al. [22] developed a finite element model to simulate the selective laser melting process. The authors considered the optical penetration depth and found that variations in speed led to different rates of change in the width and depth of the melt pool.

More recently, Nan et al. [23] adopted a numerical simulation method to investigate the powder flow during additive manufacturing powder spreading. Their study showed that the mass flow rate through the gap increased linearly with gap height, and that the critical blade spreading speed could be examined by comparing the gravity inertial timescale and the spreading inertial timescale.

The above review of the state of the art indicates that previous studies have either developed novel DEM models to simulate the powder bed in additive manufacturing or have studied the effects of particle size and spreader type on the powder bed characteristics. The present work however has focused on the optimisation of powder layer thickness while the particle size distribution was fixed in laser AM. The microstructure and mechanical property of the fabricated HX parts under the optimum process parameters were also investigated. This paper addresses this knowledge gap by using DEM to study the interactions between the particles, the wiper and the build plate during the powder deposition process. The aim is to develop an improved understanding of the effect of powder layer thickness on powder bed characteristics and to provide practical insights into the selection of optimum process parameters in laser AM.

2. Simulation setup and experimental procedures

2.1. Discrete element method

The powder deposition model and powder spreading simulation were developed using DEM. In order to investigate the effect of powder layer thickness on various powder bed characteristics, both premier layer and multi-layer powder deposition were simulated. The model uses a square build plate of 2 x 2 x 0.3 mm and a simplified wiper with a radius of 0.25 mm (Fig. 1a). The total running time of a build with *n* layers of powder may be expressed as:

$$T_n = nT_1 + (n-1)T_b \qquad (1)$$

where T_1 represents the running time of the premier layer and T_b denotes the time of the wiper moving back. T_1 and T_b may be determined as follows:

$$T_1 = \frac{S}{v_f} + T_q + T_p \qquad (2)$$

$$T_b = \frac{S}{v_b} \qquad (3)$$

where T_q and T_p represent the build plate's moving down time and powder generating time in every single cycle, respectively; v_f and v_b denote the speed of the wiper moving forward (spreading powder) and back, respectively; S is the distance moved by the wiper in a single cycle, which may be expressed as:

$$S = d + l_1 + l_2 + l_3 \qquad (4)$$

where d is the wiper width, l_1 denotes the width of the powder chamber, and l_2 and l_3 represent the dimensions of the build plate and the surrounding wall, respectively.

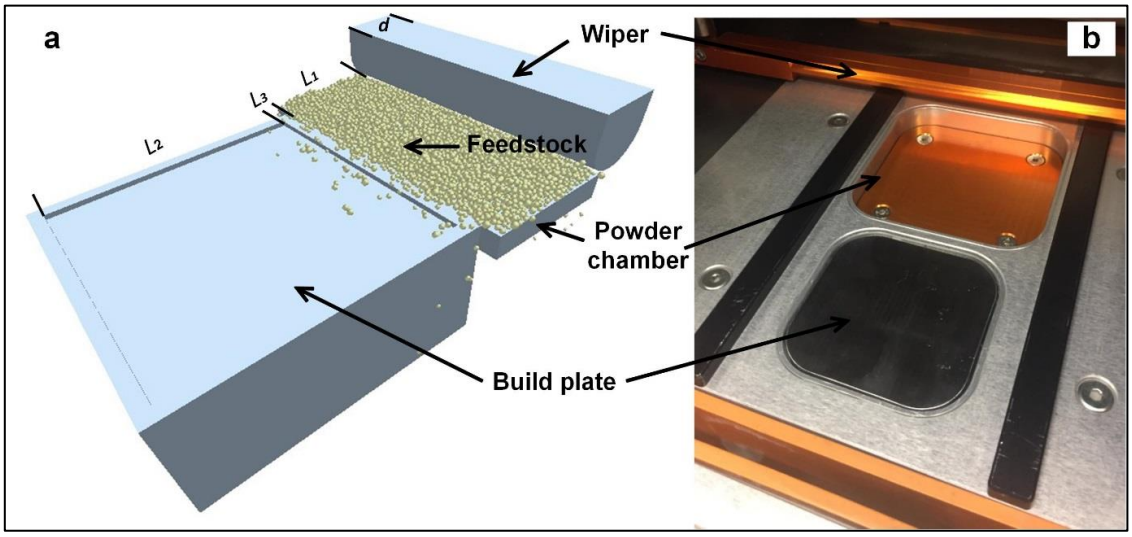

Fig. 1. Simulation (a) and experimental setup (b)

The parameters chosen in the DEM simulation are shown in Table 1.

Table 1

Discrete element simulation parameters.

Parameters	Value	Parameters	Value
Wiper width, d	0.5 mm	Wiper moving forward speed, v_f	0.018 m/s
Powder chamber width, l_1	1 mm	Wiper moving back speed, v_b	0.36 m/s
Build plate width, l_2	2 mm	Powder generating time, T_p	0.01 s
Wall thickness, l_3	0.1 mm	Build plate moving down time, T_q	0.01 s

The simulated particles are spheres (which were assumed to follow a Gaussian distribution) and had a mean particle size of 35 μm (Fig. 2a). The mean particle size is a volume based arithmetic average particle size using the laser diffraction method. Three layer thickness values (30, 40 and 50 μm) were simulated to investigate the effect of layer thickness on powder bed characteristics (Fig. 2b). The expectation is that a thin layer thickness (e.g. of 30 μm) could push the majority of the particles out of the build plate, while a much larger thickness value (e.g. 50 μm) requires a much higher laser energy input. However, due to the high thermal conductivity of metal powder, a quick heat dispersion takes place and the accumulated heat may not be able to fully melt the deposited powder.

In practical laser AM process, the ideal layer thickness is the diameter value of the used metal powder. The commercial metal powder generally follows a Gaussian distribution, an ideal layer thickness value could be slightly higher than the average particle size, because a smaller layer thickness scenario may lead to the majority of particles being pushed out of the build plate and also increases the manufacture time and cost. A larger value however may result in an insufficient melting defect due to the quick dispersion of the heat input. Considering the average particle size of 35 μm, the hypothesis of this work hence is that a 40 μm layer thickness may offer a more suitable powder bed for laser AM compared to the 30 μm and 50 μm values. Under the three cases simulation, the initial number of particles in the heap was the same and maintained at 4,000.

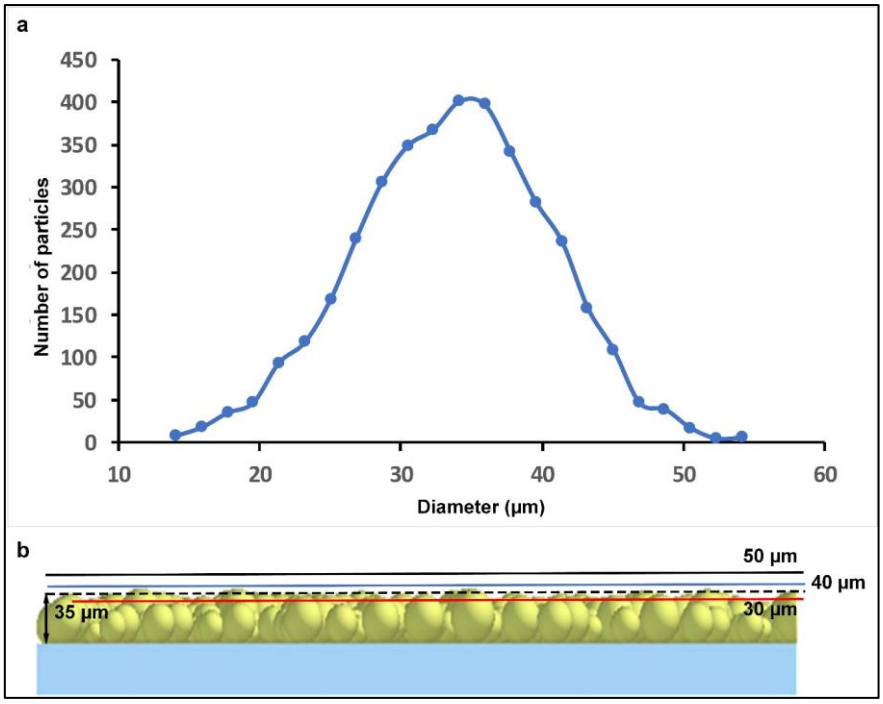

Fig. 2. Schematic diagram of the criteria for layer thickness selection.

The contact model for particles is Hertz-Mindlin with Johnson-Kendall-Roberts (JKR) cohesion, which accounts for the influence of Van der Waals forces within the contact zone [24]. The normal elastic contact force is expressed in this model as follows:

$$F_{JKR} = -4\sqrt{\pi\gamma E^*}a^{\frac{3}{2}} + \frac{4E^*}{3R^*}a^3 \tag{5}$$

where E^* is the equivalent Young's modulus; R^* and γ represent the equivalent radius and surface energy, respectively; and a denotes the contact radius. E^* and R^* may be determined as [24] [25]:

$$\frac{1}{E^*} = \frac{1-{v_i}^2}{E_i} + \frac{1-{v_j}^2}{E_j} \tag{6}$$

$$\frac{1}{R^*} = \frac{1}{R_i} + \frac{1}{R_j} \tag{7}$$

where E_i, v_i, R_i and E_j, v_j, R_j denote the Young's modulus, Poisson's ratio and radius of each sphere in contact, respectively. Additionally, there is a damping force ${F_n}^d$ given by [25]:

$${F_n}^d = -2\sqrt{\frac{5}{6}}\beta\sqrt{S_n m^*}{v_n}^{rel} \tag{8}$$

where m^* is the equivalent mass, ${v_n}^{rel}$ is the normal component of the relative velocity and β and S_n (the normal stiffness) can be expressed as [25] [26]:

$$\beta = \frac{-ln\lambda_1}{\sqrt{ln^2\lambda_1+\pi^2}} \quad (9)$$

$$S_n = 2E^*\sqrt{R^*\delta_n} \quad (10)$$

where λ_1 is coefficient of restitution and δ_n represents the normal overlap. The tangential force F_t depends on the tangential overlap δ_t and the tangential stiffness S_t and can be given by [25]:

$$F_t = -S_t\delta_t \quad (11)$$

In addition, the tangential damping is expressed as [25]:

$${F_t}^d = -2\sqrt{\frac{5}{6}}\beta\sqrt{S_t m^*}{v_t}^{rel} \quad (12)$$

where ${v_t}^{rel}$ is the relative tangential velocity; the tangential force is limited by coulomb friction $\lambda_2 F_n$ where λ_2 is the coefficient of sliding friction. The rolling friction is accounted for by applying a torque to the contacting surfaces, and the torque may be expressed as [25]:

$$\tau_i = -\lambda_3 F_n D_i \omega_i \quad (13)$$

where λ_3 is the coefficient of rolling friction, D_i and ω_i denote the distance of the contact point from the centre of mass and the unit angular velocity vector of the object at the contact point, respectively.

The parameters used in the DEM simulations were determined through the modelling calibration and relevant literature. The DEM simulations often use an effective modulus, which is up to 2 orders of magnitude lower than the elastic constants for the real material in the DEM force-displacement relation [16]. The values of Young's modulus and Poisson's ratio were set to 2 GPa and 0.31 for all particles which are typical values for HX alloy powder [27]. The coefficient of restitution and the coefficient of sliding friction are set to $\lambda_1 = 0.4$ and λ_2 =0.4, respectively, which are chosen based on the basis of Meier et al. [18], in which a DEM model was developed

to predict the angle of repose (AOR) of titanium powder by considering the frictional contact, rolling resistance and cohesive force. The spherical HX powder used in present study exhibits the same average particle size (34 μm) and similar powder density (5000 kg/m^3) compared to the rigid titanium powder in [18]. The coefficient of rolling friction is set to $\lambda_3 = 0.005$ for all the simulations on the basis of Zhou et al. [28] to generate a travelling distance of approximately 20 R^*. Because particles are deposited on the powder bed which is not smooth, the particles are thus not expected to roll for long distance [15]. In the absence of experimental measurements this is a reasonable presumption. The determination of AOR and surface energy γ will be detailed in next section.

2.2. Model calibration

The calibration of surface energy is crucial because adhesion forces exist in the fine metallic powder such as electrostatic attraction and van der Waals interactions, which significantly affect the powder's flow performance. When the particle size was less than 100 μm, the van der Waals force was found to dominate the electrostatic force by orders of magnitude for conductive powders [29] [30]. In order to calibrate the surface energy, the AOR was determined using physical funnel experiments and to match the numerical simulations. A detailed method used for surface energy calibration may be found in [18] and this method was also adopted in present study.

In order to study the sensitivity of surface energy with respect to the cube side length, three different side length values (a = 10 mm, 5 mm and 2.5 mm) were used and the measured funnel results are shown in Fig. 3. The AOR was measured by fitting an isosceles triangle (red solid lines) to each 2D image. The cube side length was found to have no apparent influence on the AOR; the AOR value under each case was measured to be 31.8º, 33.1º and 32.1º, respectively. The average value 32º was thus used in present study.

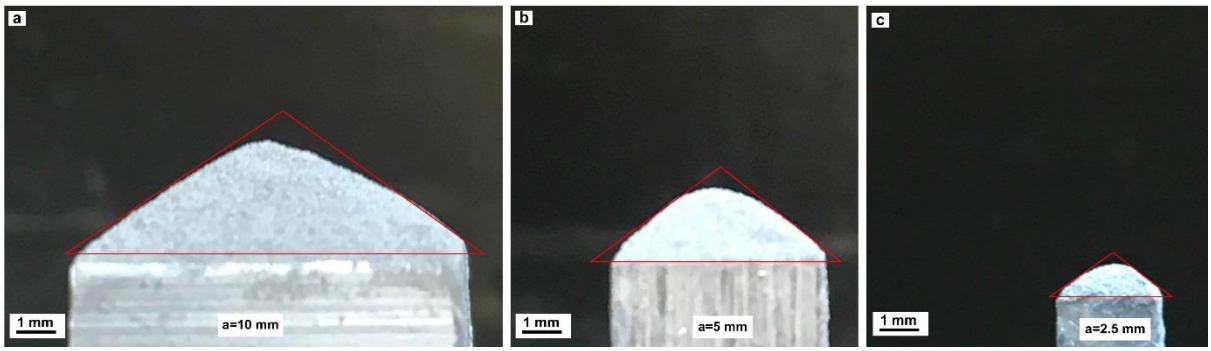

Fig. 3. Experimental funnel results for HX powder with different edge length values

Fig. 4 reveals the numerically simulated 2D projections of powder piles and derived AOR with respect to the surface energy that varied from 0 to 2 mJ/m^2. Likewise, the AOR value was measured by fitting an isosceles triangle (red solid lines) to each 2D image. As expected, the AOR increases with an increase in surface energy (i.e. increasing the cohesiveness of powder); the AOR was determined to be 8º under a 0 mJ/m^2 surface energy while the value increased to 38º under the 2 mJ/m^2 surface energy. Also, it was found that a surface energy of 1.6 mJ/m^2 led to a 32º AOR, which fitted very well to the experimental results (Fig. 3). The $\gamma = 1.6\ \mathrm{mJ}/m^2$ was thus adopted in the simulations in present study.

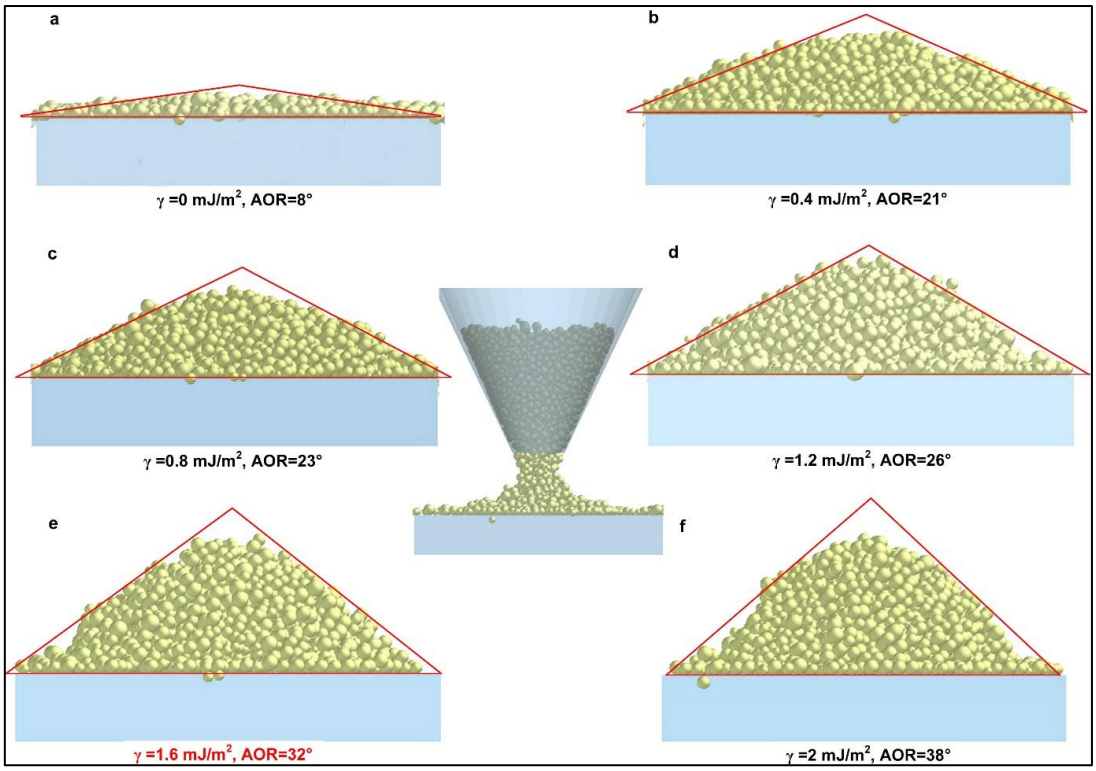

Fig. 4. 2D projections of the powder piles and derived AOR values from numerical funnel simulations with different surface energy values.

2.3. Laser additive manufacturing (AM) and characterisation techniques

The material used in this study was Hastelloy X (HX) alloy, acquired from Sandvik Osprey (Neath, UK). The average particle size (D_{50}) was measured to be 34.4 μm, with a D_{10} of 22.5 μm and D_{90} of 52.3 μm. A Renishaw AM250 system (Gloucestershire, UK) with a modulated ytterbium fibre laser with a wavelength of 1071 nm was used to manufacture the samples. Once the optimum powder layer thickness was determined, the other main process parameters were optimised by measuring the relative density of the as-fabricated cubic samples (10 x10 x 10 mm), which was found to be greater than 99.5%. The relative density is the ratio of experimentally measured density to the given reference density (8.22 g/cm^3 for fully dense HX alloy). The tensile specimens were fabricated horizontally; their dimensions were determined according to ASTM-E8/E8M-13a [31].

The cubic samples were vertically sectioned, ground and then polished (3 μm, 1 μm diamond suspension and OPS colloidal silica, 0.04 μm) using standard techniques prior to optical microscopy for defects inspection. For the microstructure analysis, the polished samples were electrochemically etched using oxalic acid for 10s to reveal molten pool boundaries and solidification structures. The uniaxial tensile tests were performed using a Zwick/Roell tester with a strain rate of 2 mm/min at room temperature. The engineering stress-strain curves were obtained based on two tensile samples.

3. Results and discussion

3.1. Premier layer and multi-layer simulation

3.1.1. Powder bed characteristics during premier layer deposition

Fig. 5 shows the simulated powder bed after the premier layer's deposition (T = 0.21 s) using the same three layer thickness values. Prior to the three cases deposition, a 0-micrometer layer thickness condition was conducted to validate the model and it revealed that all the particles were pushed out of the build plate as expected. As Fig. 5a (30 μm) shows, several large voids formed; they were uniformly distributed on the build plate and varied in size between 0.03 mm^2 and 0.1 mm^2. The 40 μm and 50 μm cases also contributed to voids formation but their size is much smaller. One should also note that the number of particles for spreading, initially set to 4,000, was reduced

to 360 after the deposition process (Fig. 5d). With an increase in the layer thickness to 40 μm and 50 μm, this value increased to 1,578 and 1,898, respectively (Fig. 5b-d). This finding suggests that layer thickness is one primary factor to affect the powder bed characteristics when the employed powder exhibits a good flowability. Indeed, the experimentally measured AOR in present work is around 32° (less than 40°), implying the commercial HX powder flows well.

Clearly, when the layer thickness that is employed (e.g. 30 μm) is less than the mean particle size (35 μm), more than 85% of particles are pushed out of the build plate by the wiper, and a large number of voids are thus formed, which is detrimental to the dimensional accuracy and mechanical properties of the final components, as observed in a previous study [24]. On the other hand, when the layer thickness was greater than the mean size, the deposited premier layer's powder exhibited more uniform distribution on the build plate (Fig. 5b-c), compared to the 30 μm condition although this uniformity also led to the formation of a 'rebound zone'. This rebound zone formed as a result of the compressive force between the wiper, the particles and the build plate wall. More specifically, the spreading powder was subject to a compressive force from the wiper and when the powder approached the build plate wall, the compressed particles rebounded and formed the rebound zone.

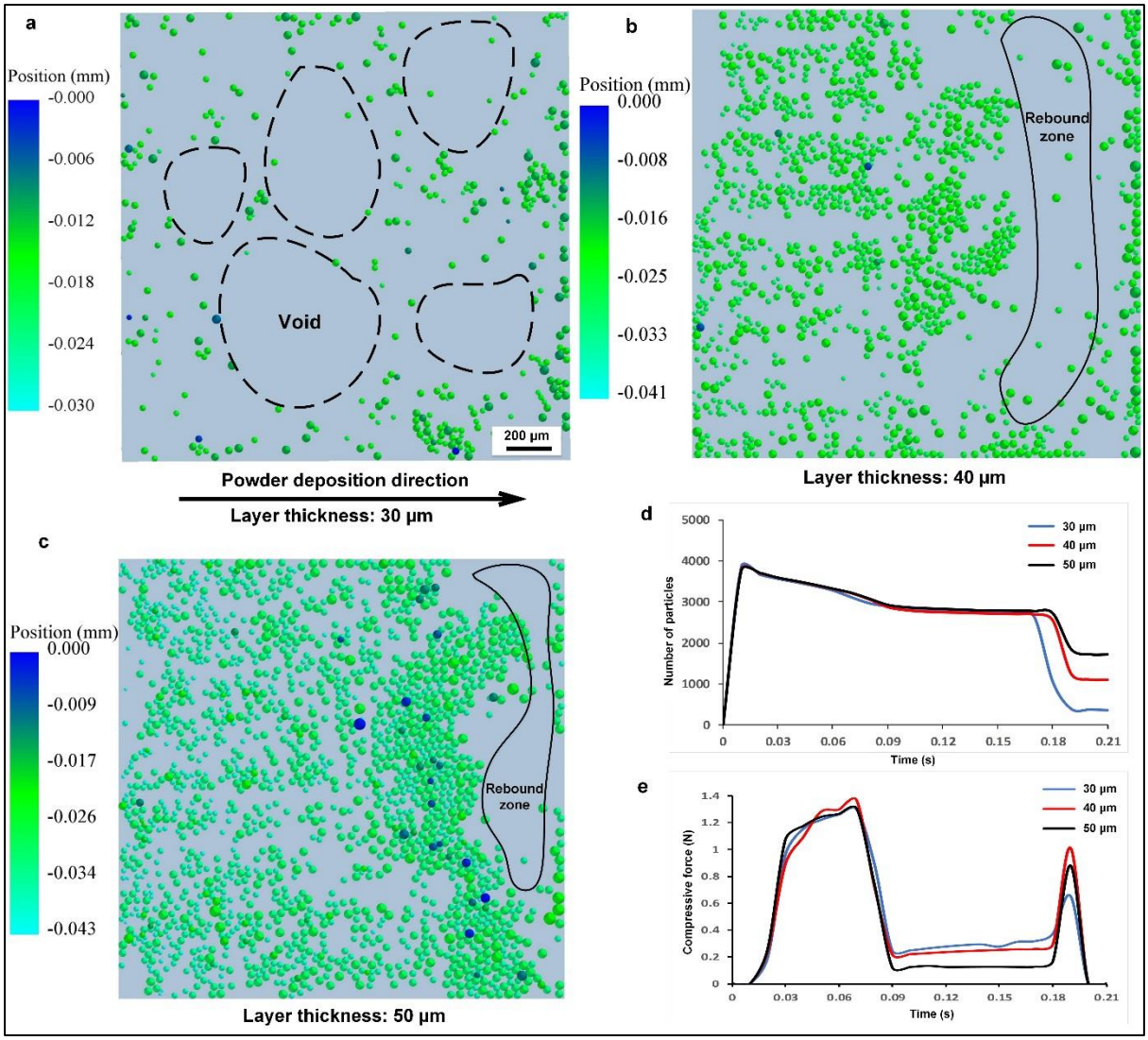

Fig. 5. The premier layer's powder bed characteristics under different layer thickness values.

Fig. 5e shows the simulated compressive force with respect to the running time. Once the powder generation was complete (after 0.01 s), the compressive force started to increase in all cases (30 µm, 40 µm and 50 µm) until reaching a peak at 0.07 s. This finding may be explained by the fact that during this period, the wiper applied a compressive force to spread the particles on the powder chamber plate. The compressive force gradually increased until reaching a maximum of 1.3 N. When the wiper moved into the build plate, the compressive force was reduced significantly once a new layer was deposited. The 30 µm and 40 µm layer thickness cases exhibited very similar compressive performance and generated compressive forces of 0.24 N and 0.21 N, respectively, while the 50 µm case produced a much lower compressive force

(0.12 N; 0.09 s). The compressive force then tended to stabilise until the wiper reached the build plate wall (at 0.19 s).

The compressive force showed another significant increase again for all cases, which occurred because of the number of particles compressed between the wiper and the build plate wall at this stage. Once the wiper moved out of the build plate, the compressed particles rebounded, which led to the formation of a rebound zone (Fig. 5b-c). On one hand, one can keep the part's cross-section smaller than the build plate to avoid the rebound zone in practical laser AM process, but on the other hand, this may result in a waste of the build volume in some degree and an increase in build cost.

3.1.2. Powder bed characteristics during multi-layer deposition

Fig. 6 shows the powder bed characteristics after three consecutive layers of powder deposition (30 µm, 40 µm and 50 µm of layer thickness). The x-y image shows the top view, while the x-z image represents the side view. Similarly to the premier layer deposition discussed in the previous section, voids were also generated in the powder bed, but the void size was much smaller than the voids observed in the premier layer deposition. The maximum position value (e.g. height) of the deposited powder was around -0.083 mm when the mean particle size was 35 µm. The 40 µm layer thickness enabled a more uniform particle distribution on the powder bed (Fig. 6b). A very limited number of micro-voids were generated because the deposited particles interacted with each other through the space filling and minimised void creation, thereby improving the powder bed quality.

With a further increase in the layer thickness to 50 µm, the maximum position value increased from -0.113 mm to -0.143 mm (Fig. 6c). Considering the Gaussian distribution of the particle (Fig. 2a), nearly all the particles could have been deposited on the build plate in every single layer's powder spreading. Short-feed defects were observed at the rear of the build plate (the end of the plate along the wiper spreading direction), however, which in general can significantly degrade the quality of the built parts and subsequently increase build costs due to the need to repeat the builds. Interestingly, the three different colours of the particles (blue, green and red) indicated the particles' distributions on the first, second and third layers, respectively.

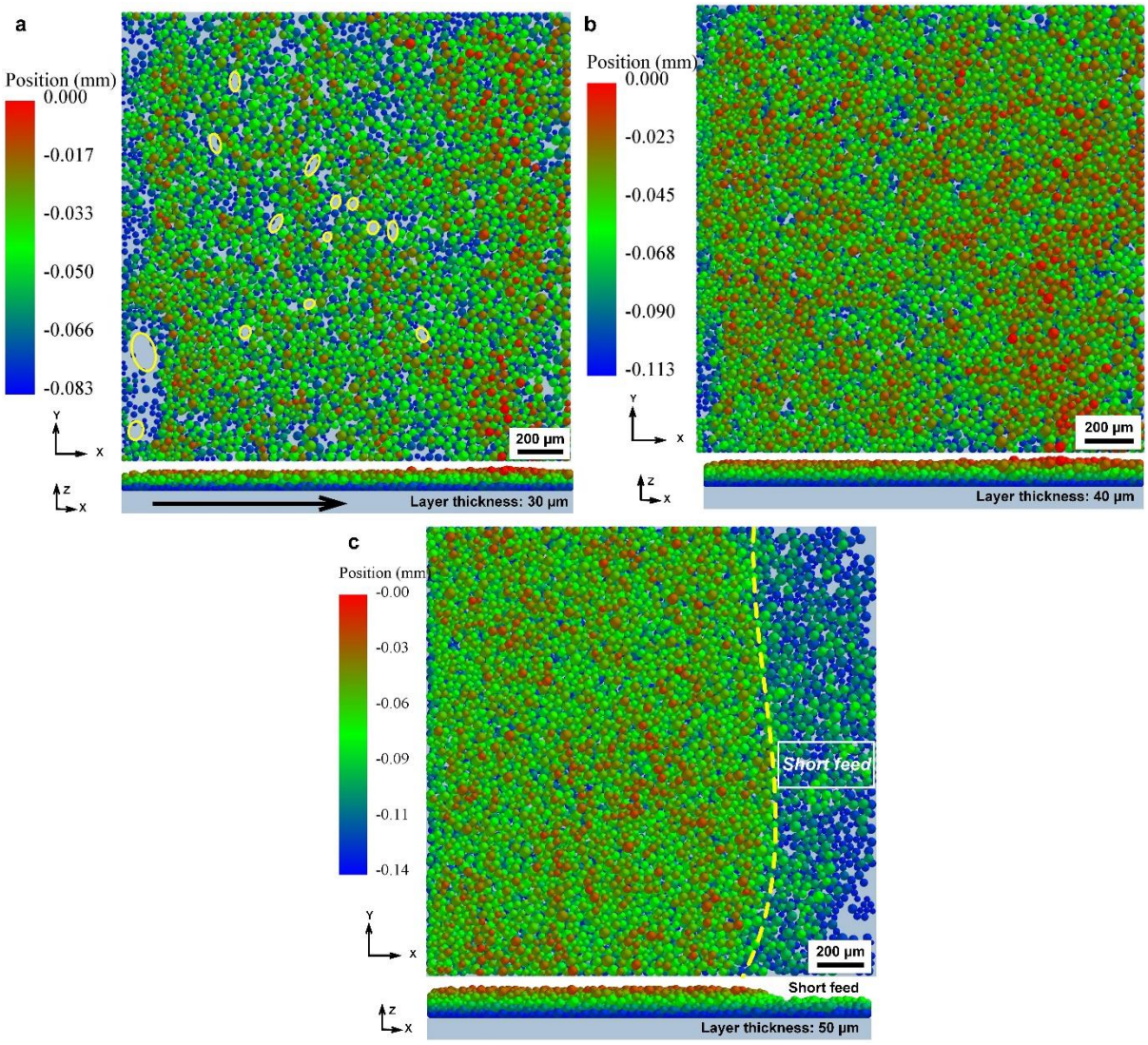

Fig. 6. Multi-layers' powder bed characteristics under different layer thickness values.

As a further aid to investigating the influence of layer thickness on powder bed characteristics, Fig. 7 shows the number of the deposited particles and their particle size distribution in the simulation model. The number for the mean-size (33 µm) particles varied from 560 to 1,150 when the layer thickness was increased from 30 µm to 50 µm (Fig. 7a–c). At the same time, the total number of particles deposited on the build plate varied considerably under the three thickness cases. As Fig. 5d shows, the number of deposited particles increased from 360 to 1,850 after the premier layer deposition with layer thickness values of 30 µm and 40 µm, respectively, while no significant difference was detected between the 40 µm and 50 µm cases. Once the second layer deposition was complete, the values for the deposited particles increased to 1,720 and 5,475 for the 30 µm and 40 µm cases, respectively. The difference between the 30 µm and 40 µm cases tended to be much larger after the third layer

deposition was complete; these differences were determined to be 4,580 and 9,765, respectively (Fig. 7d).

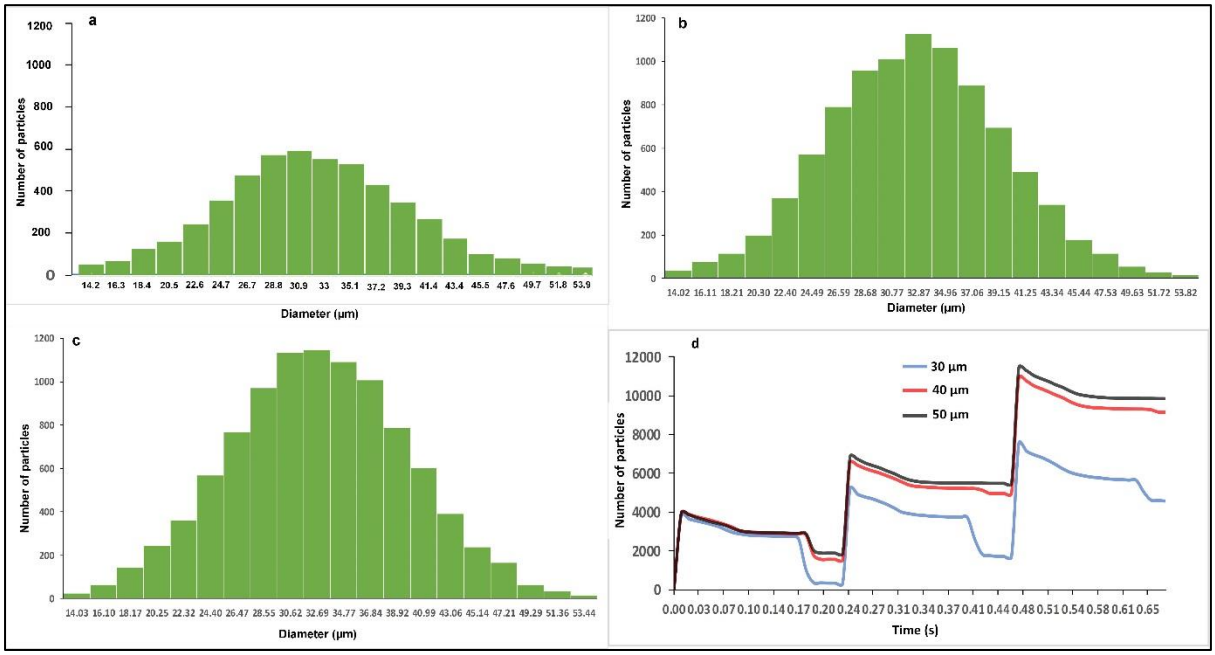

Fig. 7. Particle size distribution and numbers of deposited particles after the deposition of three layers using different layer thickness values.

The difference in the number of deposited particles may be explained by the compressive force between the wiper, the particles and the build plate; in general, this force is closely linked to the particle size distribution and layer thickness. Fig. 8 shows the theoretically calculated compressive force during the deposition of the three layers. More specifically, during the premier layer deposition on the build plate (0.09 s–0.18 s), the 30 μm layer thickness case exhibited a higher compressive force than the 40 μm and 50 μm cases (0.23 N, 0.2 N and 0.12 N, respectively). When the wiper approached the build plate wall (0.19 s), the compressive force significantly increased to 0.65 N, 1.01 N and 0.88 N (peak force), respectively. During the deposition of the second layer, the 40 μm and 50 μm cases exhibited similar compressive performance, although the 30 μm case generated a slightly higher force. The peak force took place at 0.42 s, where the 30 μm case exhibited the highest value (0.85 N). This finding suggests that when the particle size distribution is fixed (i.e. the powder is homogeneous), the layer thickness tends to affect the second layer more than the premier layer.

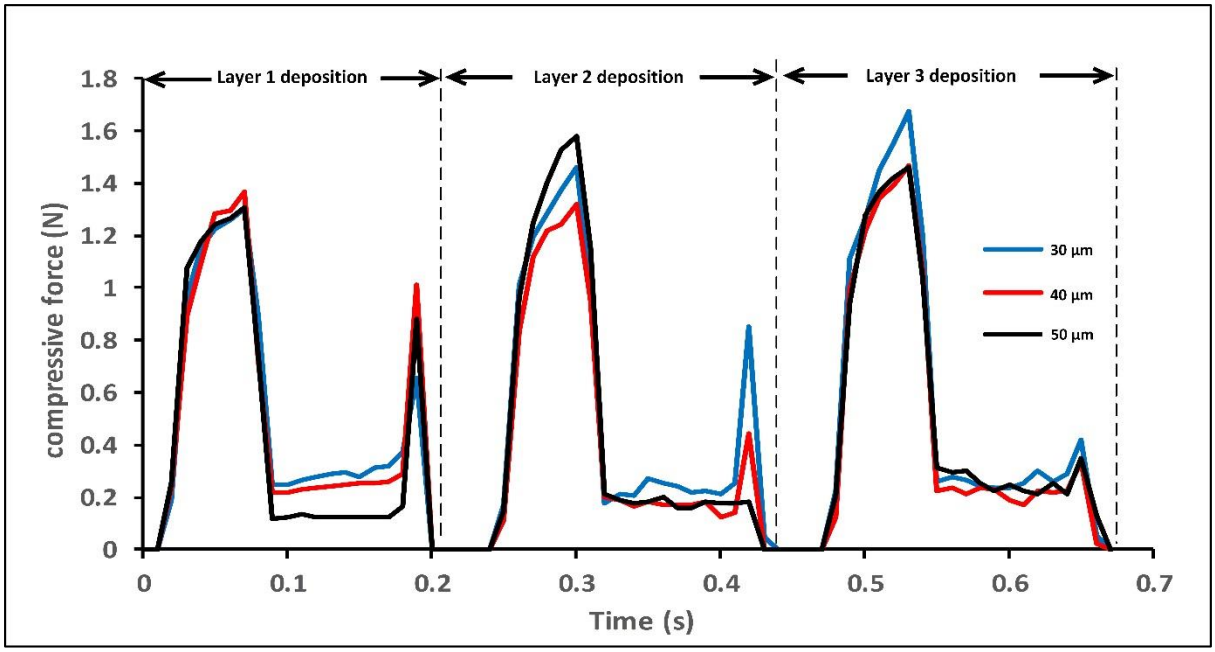

Fig. 8. Simulated compressive force within three layers powder deposition.

During the deposition of the third layer, the three cases showed very similar compressive performance, with a peak force of 0.34 N, which was much lower than that generated during the deposition of the second layer (0.85 N for the 30 µm case). This may be explained by the fact that, with an increase in the layer number (i.e. more than two layers), the gaps between the pre-deposited particles offered sufficient space to counteract the compressive force induced by the wiper, the particles and the build plate wall, implying the formed rebound zone within the first a couple of layers may disappear gradually. As has been widely reported in the literature, deposited powder beds exhibit a porosity from 20% to 40% [25] [26] [27] [32]. This fairly large porosity generally enables more particle contacts to occur during the powder spreading and is favourable to the flattening of the powder bed surface topography.

3.2. Experimental validation

Fig. 9 shows the experimentally obtained powder bed characteristics after the deposition of three layers (30 µm, 40 µm and 50 µm of layer thickness). Several voids were clearly observable when a 30 µm layer thickness value was used; the powder bed exhibited a rugged topography, which was detrimental to the next layers' deposition and dimensional accuracy for the built part. This setup showed good agreement with the simulation (Fig. 6a), which indicated the formation both of voids and of a rugged powder bed surface. When the layer thickness was increased to 40 µm and 50 µm, a much smoother powder bed surface without micro-voids was formed,

although a short-feed defect formed at the rear of the build plate, which was consistent with the simulated results. The obtained fraction of short feed zone in the deposited powder bed was around 9.1% (Fig. 9c). The short-feed defect is the shortage of powder at the end of layer-recoating while insufficient amount of powder is used. This issue could be resolved by applying a larger amount of powder per recoating, but sometimes we prefer using the minimum number of particles per recoating by reducing the dosing percentage to save powder, particularly in developing new composite materials for AM due to the high cost in materials synthesis. Therefore, identifying the optimum layer thickness is significant in order to both guarantee the built parts' quality and consume the minimum amount of powder.

On the basis of both the simulation and experimental results, one can see that when the Gaussian-distributed particles exhibited an average particle size of around 35 µm, the optimum layer thickness was 40 µm, as this thickness could contribute to a uniformly distributed powder bed without voids or short-feed defects. This finding confirms the initial hypothesis. This value was then used for the optimisation of laser energy density, which is closely linked to laser power, laser scanning speed and hatch spacing.

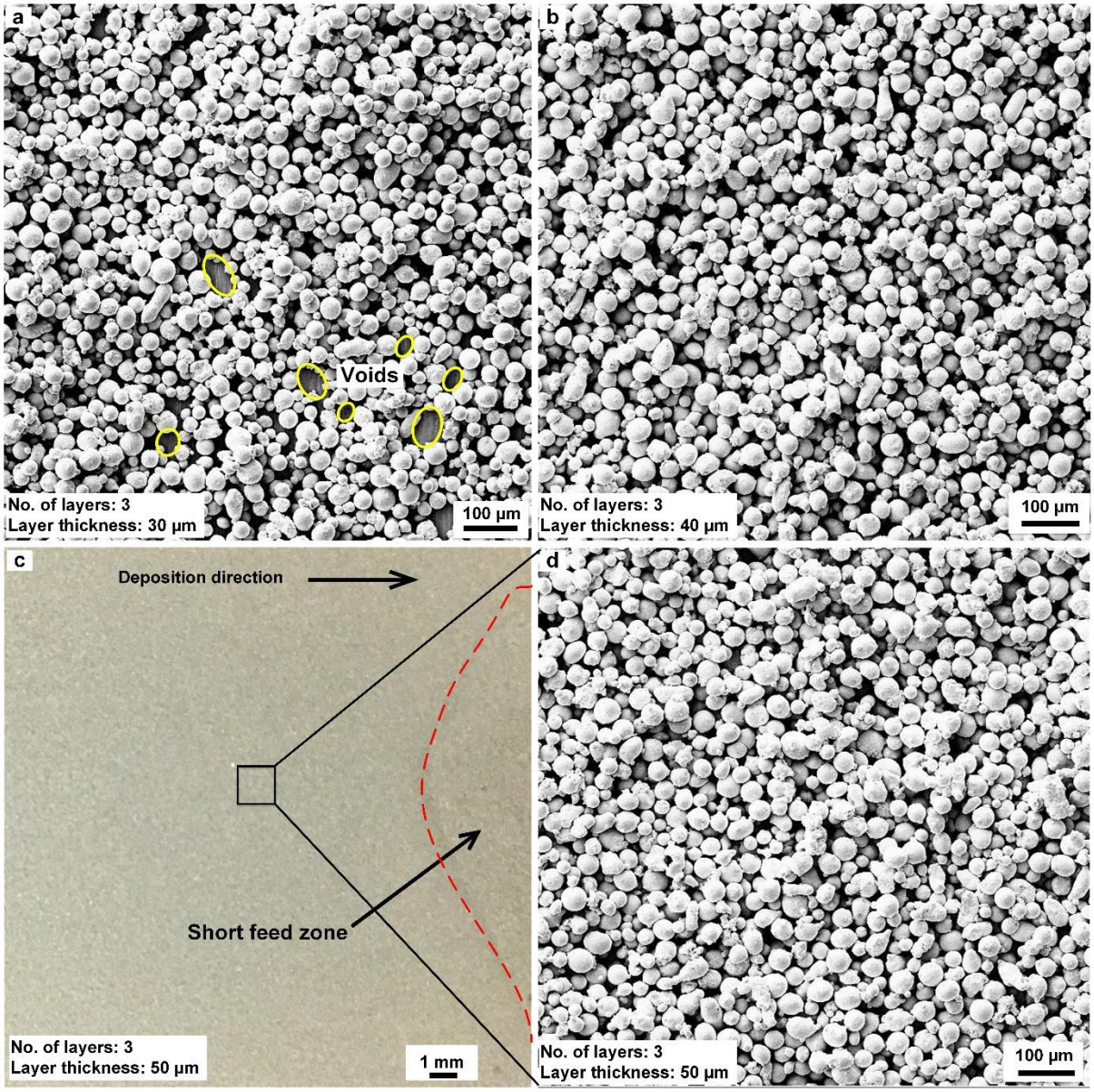

Fig. 9. Experimental validation of the theoretical model

3.3. Microstructure and tensile performance

Fig. 10 shows the relative density of the as-fabricated HX cubic samples with respect to laser energy density, which is expressed as $\varepsilon = \frac{P}{v \cdot t \cdot h}$, where P is the laser power, v donates the scanning speed, and t and h represent the layer thickness (40 μm in this study) and hatching spacing, respectively [33] [34]. As the figure shows, the relative density increased with the increase in energy density until 83.33 J/mm^3, at which point a maximum density of 99.5% was achieved. The tensile specimens used in this study were thus fabricated using several optimum process parameters (laser power: 200 W; hatch spacing: 100 μm; scanning speed: 600 mm/s; layer thickness:

40 μm), which together provide the maximum relative density. The relative density then decreased with further increases in the energy density until reaching 156.25 J/mm^3. The relatively high energy density (greater than 100 J/mm^3) induced by the low scanning speeds, however, contributed to lower relative density values. This situation may be explained by the keyhole formations in the fabricated specimens. When a relatively low scanning speed was used, a very high density of laser energy was applied to the powder bed, which led to the change of melting mechanism from conduction to 'keyhole-mode' laser melting. In this mode, the molten pool depth was controlled by the evaporation of the molten material. The vapor recoil pressure caused by the strong evaporation applied extra forces to the surface of the molten pool and resulted in molten pool depth that can be much deeper than observed in conduction mode. In addition, the collapse of the vapor cavity that was formed by the evaporation can result in the keyhole voids formation. This explains the decrease of relative density under low scanning speeds.

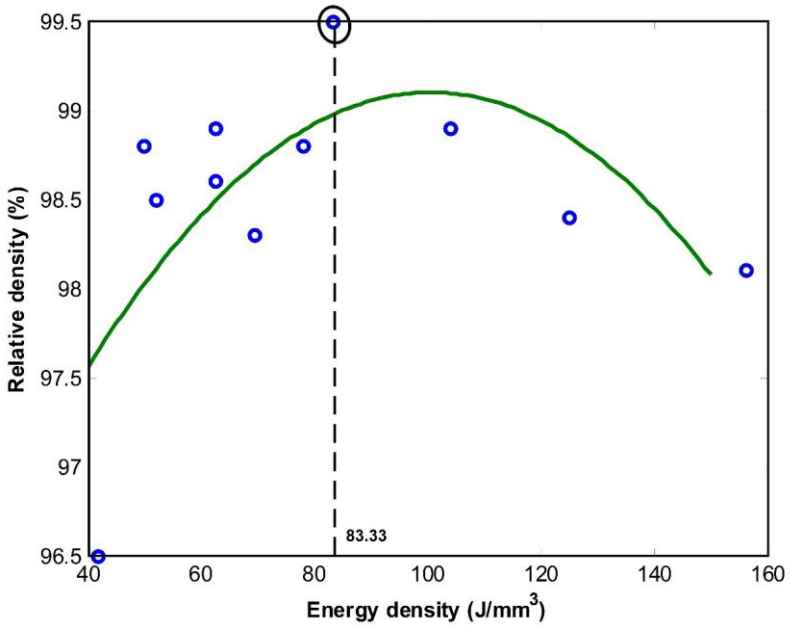

Fig. 10. Relative density with respect to laser energy density

Fig. 11 shows the microstructure of the sectioned samples under the optimum (83.33 J/mm^3) and maximum (156.25 J/mm^3) laser energy densities, respectively. A very limited number of residual pores were observed in the optimum energy density case (Fig. 11a-b), and the pore size was measured to be less than 30 μm. The molten pools that formed exhibited a very uniform shape and size; the molten pools

penetrated to the pre-solidified layers, thus contributing strong bonding behaviour between two adjacent layers. A higher energy density was not found to further increase the relative density but did contribute to the formation of large keyhole pores (Fig. 11c-e). Several very deep molten pools were also observed that managed to penetrate a few solidified layers. Compared to the residual pores, the keyhole pores exhibited much larger dimensions; the pores were measured to be around 70 μm in diameter.

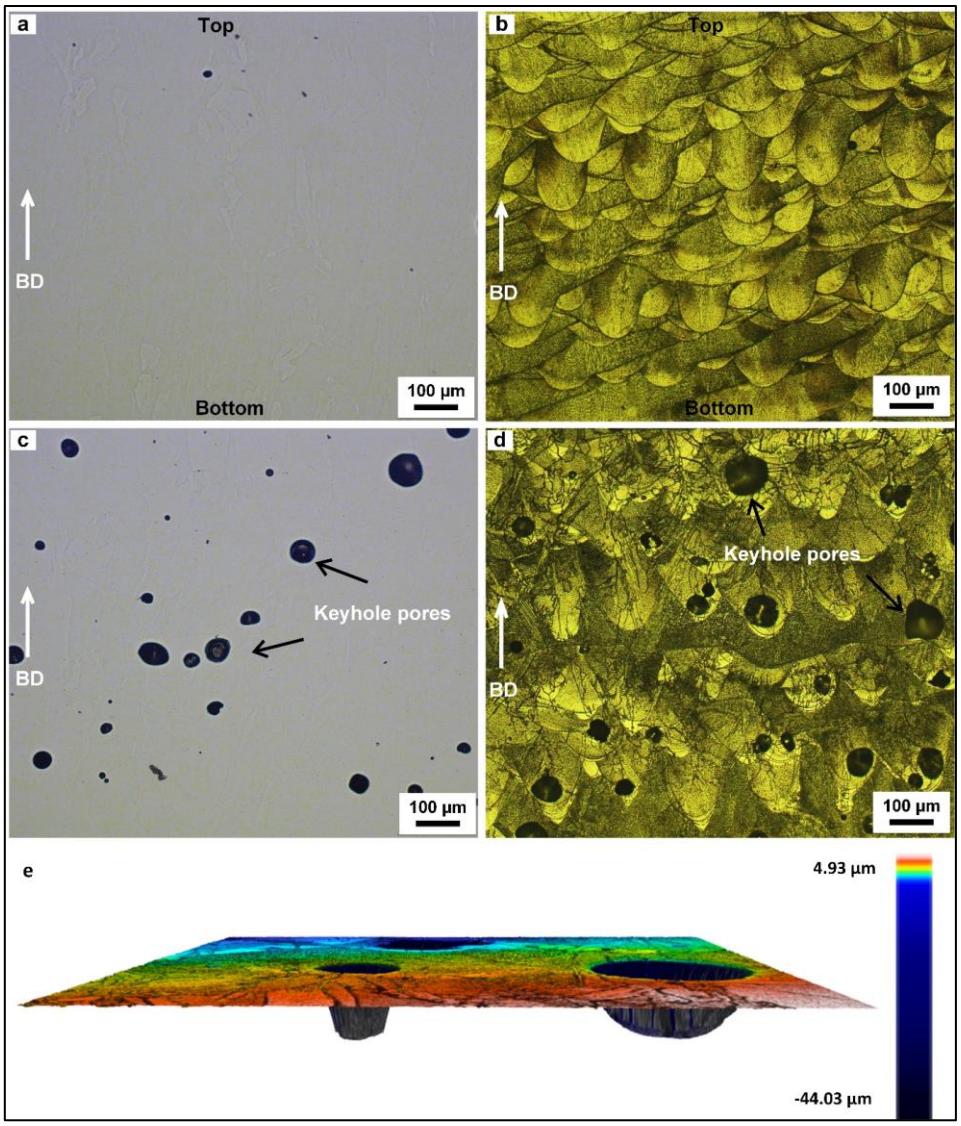

Fig. 11. Porosity and microstructure under different energy densities: (a-b) 83.33 J/mm^3; (c-e) 156.25 J/mm^3.

In addition to the 2D analysis, the depth of the keyhole pores was also measured and was found to be around 44 μm (Fig. 11e). The keyhole pores that were generated were found to have exhibited spherical rather than irregular shapes. Indeed, under the keyhole conduction mode that was induced by the relatively low scanning speed, when

the molten pool surface temperature approached the boiling temperature, a strong evaporation of the molten material took place, which produced a vapor recoil pressure and this pressure applied an exponentially increasing force normal to the surface. The keyholes formed because of the collapse of vapor cavity at the solidification stage. More details on the formation of keyhole pores may be referred to in several previous works [35] [36] [37].

Fig. 12 shows the measured tensile performance of the as-fabricated HX samples under the optimum processing conditions. The tensile performances of the two as-fabricated tensile specimens were found to be very consistent, with a 600 ± 5 MPa yield strength, 765 ± 3 MPa ultimate tensile strength, and 29± 3% elongation (Fig. 12a). Necking was observed at the fracture surface following the tensile test. The high elongation (29%) observed implies that the samples showed ductile rather than brittle fracturing during testing.

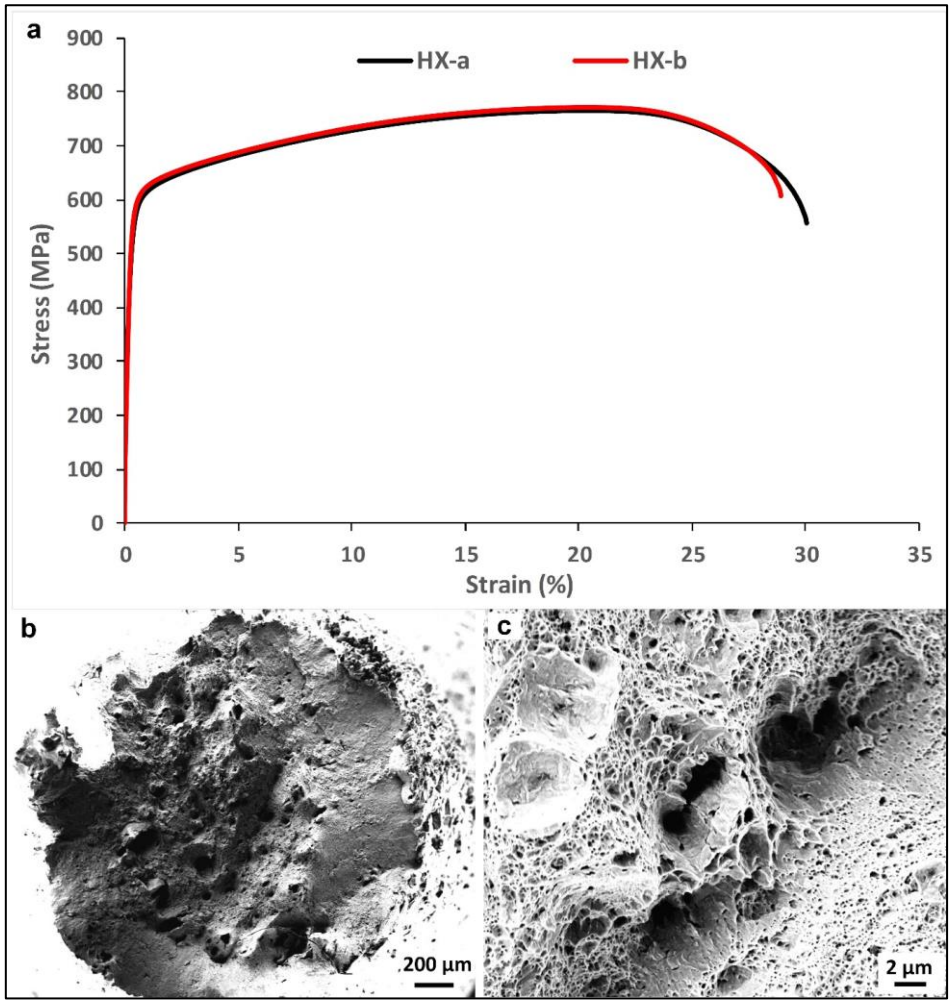

Fig. 12. Tensile performance of the as-fabricated HX specimens under optimum energy density.

The images in Fig. 12b-c show the fracture surfaces following tensile testing. The open pores that formed were further opened under the uniaxial loading. It should be noted that the opened pores exhibited irregular shapes rather than the circular shapes that were observed on the sectioned surface. The dendritic features were not observed in the fracture surfaces, which differs from the previous findings of a previous study on additive-manufactured HX alloys [11]. In that study, cleavage-like surfaces were observed, indicating that the columnar grains were elongated along the loading direction. This difference may be explained by the fact that the tensile samples were horizontally built in the present study (perpendicular to the loading direction), while the specimens used in [11] were fabricated vertically (parallel to the loading direction).

4. Conclusions

This study has investigated the effect of layer thickness on various powder bed characteristics in the laser additive manufacturing (AM) process. These effects were validated through an experimental study of the microstructure and tensile performance of Hastelloy X samples, which were manufactured using optimised parameters determined by the study's improved understanding of the effect of layer thickness. The study has generated several important findings:

(1) During the deposition of the premier layer, more than 85% of the particles were pushed by the wiper out of the build plate when the layer thickness (30 μm) was less than the mean particle size (35 μm). In contrast, the 40 μm and 50 μm layer thickness cases enabled uniform particle distribution on the build plate, although a 'rebound zone' was formed; this zone was induced by the compressive force between the wiper, the particles and the build plate wall.

(2) During the multi-layer deposition, voids were found (both theoretically and experimentally) to have formed on the powder bed under the 30 μm layer thickness condition, while a more uniform powder bed was obtained under the 40 μm condition; the 50 μm layer thickness, however, was found to have resulted in short-feed defects. The optimised layer thickness could be further used for the optimisation of other parameters.

(3) The compressive force was found to be significantly layer-dependent. The force tended to be consistent in all three cases when three layers were used, which suggests that, when the average particle size was fixed at 35 μm, from the point

of view of powder bed uniformity, the three layer thickness cases (30 μm, 40 μm and 50 μm) that were used could offer a uniform powder bed when more than three layers are used.

(4) A very limited number of residual pores formed under the optimum laser energy density, while a further increase in energy density contributed to the formation of keyholes. The optimum-condition fabricated HX samples exhibited a 600 ± 5 MPa yield strength, a 765 ± 3 MPa ultimate tensile strength and 29 ± 3% elongation.

These results indicate that layer thickness plays a significant role in determining powder bed characteristics in the laser AM process. The compressive force that was applied to the particles tended to be very low and consistent and a uniform powder bed could be offered under the three layer thickness conditions when three layers of particles were deposited, thus implying that the number of layers is not the only important factor for powder bed porosity. Therefore, the future work should focus on other parameters that may affect the powder bed characteristics. For instance, the effects of temperature on both powder's flowability and surface energy need to be further investigated. This is because the laser energy input heats the powder bed and the temperature rises with an increase in layer number; when a new layer of powder is deposited, the increased temperature on both the powder bed and solidified parts might affect the powder flowability and surface energy.

In conclusion, this study has provided an improved understanding of the powder deposition process and offers insights into the selection of suitable powder layer thicknesses and other process parameters within laser AM. Future work will include validating the theoretical model with other materials and expanding it to model metal-matrix composites for additive layer manufacturing.

Acknowledgements

The authors would like to thank Mr Richard Thomas of Cardiff University for the tensile testing operations used in the study. The authors also appreciate the financial support of ASTUTE 2020 and ASTUTE East at Cardiff University, which made possible this research.

References

[1] J.-P. Kruth, P. Mercelis, J. Van Vaerenbergh, L. Froyen, M. Rombouts, Binding mechanisms in selective laser sintering and selective laser melting, Rapid Prototyp. J. 11 (2005) 26–36. doi:10.1108/13552540510573365.

[2] O.L.A. Harrysson, O. Cansizoglu, D.J. Marcellin-Little, D.R. Cormier, H.A. West, Direct metal fabrication of titanium implants with tailored materials and mechanical properties using electron beam melting technology, Mater. Sci. Eng. C. 28 (2008) 366–373. doi:10.1016/j.msec.2007.04.022.

[3] Q. Han, Y. Geng, R. Setchi, F. Lacan, D. Gu, S.L. Evans, Macro and nanoscale wear behaviour of Al-Al2O3 nanocomposites fabricated by selective laser melting, Compos. Part B Eng. 127 (2017) 26–35. doi:10.1016/j.compositesb.2017.06.026.

[4] Z. Sun, X. Tan, S.B. Tor, W.Y. Yeong, Selective laser melting of stainless steel 316L with low porosity and high build rates, Mater. Des. 104 (2016) 197–204. doi:10.1016/j.matdes.2016.05.035.

[5] H. Attar, S. Ehtemam-Haghighi, D. Kent, X. Wu, M.S. Dargusch, Comparative study of commercially pure titanium produced by laser engineered net shaping, selective laser melting and casting processes, Mater. Sci. Eng. A. (2017). doi:10.1016/j.msea.2017.08.103.

[6] A. Sarker, N. Tran, A. Rifai, J. Elambasseril, M. Brandt, R. Williams, M. Leary, K. Fox, Angle defines attachment: Switching the biological response to titanium interfaces by modifying the inclination angle during selective laser melting, Mater. Des. (2018). doi:10.1016/j.matdes.2018.05.043.

[7] N.T. Aboulkhair, I. Maskery, C. Tuck, I. Ashcroft, N.M. Everitt, Improving the fatigue behaviour of a selectively laser melted aluminium alloy: Influence of heat treatment and surface quality, Mater. Des. (2016). doi:10.1016/j.matdes.2016.05.041.

[8] Q. Han, R. Setchi, F. Lacan, D. Gu, S.L. Evans, Selective laser melting of advanced Al-Al2O3 nanocomposites: Simulation, microstructure and mechanical properties, Mater. Sci. Eng. A. 698 (2017) 162–173. doi:10.1016/j.msea.2017.05.061.

[9] Q. Han, H. Gu, S. Soe, R. Setchi, F. Lacan, J. Hill, Manufacturability of AlSi10Mg overhang structures fabricated by laser powder bed fusion, Mater. Des. (2018). doi:10.1016/j.matdes.2018.10.043.

[10] S. Catchpole-Smith, N. Aboulkhair, L. Parry, C. Tuck, I.A. Ashcroft, A. Clare, Fractal scan strategies for selective laser melting of 'unweldable' nickel superalloys, Addit. Manuf. (2017). doi:10.1016/j.addma.2017.02.002.

[11] Q. Han, R. Mertens, M. Montero-Sistiaga, S. Yang, R. Setchi, K. Vanmeensel, B. Hooreweder, S.L. Evans, H. Fan, Laser powder bed fusion of Hastelloy X: effects of hot isostatic pressing and the hot cracking mechanism, Mater. Sci. Eng. A. 732 (2018) 228–239. doi:https://doi.org/10.1016/j.msea.2018.07.008.

[12] A.T. Sutton, C.S. Kriewall, M.C. Leu, J.W. Newkirk, Powder characterisation techniques and effects of powder characteristics on part properties in powder-bed fusion processes, Virtual Phys. Prototyp. 12 (2017) 3–29. doi:10.1080/17452759.2016.1250605.

[13] S. Haeri, Optimisation of blade type spreaders for powder bed preparation in Additive Manufacturing using DEM simulations, Powder Technol. 321 (2017) 94–104. doi:10.1016/j.powtec.2017.08.011.

[14] E.J.R. Parteli, T. Pöschel, Particle-based simulation of powder application in additive manufacturing, Powder Technol. 288 (2016) 96–102. doi:10.1016/j.powtec.2015.10.035.

[15] S. Haeri, Y. Wang, O. Ghita, J. Sun, Discrete element simulation and experimental study of powder spreading process in additive manufacturing, Powder Technol. 306 (2017) 45–54. doi:10.1016/j.powtec.2016.11.002.

[16] E.B. Herbold, O. Walton, M.A. Homel, Simulation of Powder Layer Deposition in Additive Manufacturing Processes Using the Discrete Element Method, LLNL-TR-678550. (2015). doi:10.2172/1239200.

[17] C. Meier, R. Weissbach, J. Weinberg, W.A. Wall, A.J. Hart, Critical influences of particle size and adhesion on the powder layer uniformity in metal additive manufacturing, J. Mater. Process. Technol. (2019). doi:10.1016/j.jmatprotec.2018.10.037.

[18] C. Meier, R. Weissbach, J. Weinberg, W.A. Wall, A. John Hart, Modeling and characterization of cohesion in fine metal powders with a focus on additive manufacturing process simulations, Powder Technol. (2019). doi:10.1016/j.powtec.2018.11.072.

[19] H.W. Mindt, M. Megahed, N.P. Lavery, M.A. Holmes, S.G.R. Brown, Powder Bed Layer Characteristics: The Overseen First-Order Process Input, Metall. Mater. Trans. A Phys. Metall. Mater. Sci. (2016). doi:10.1007/s11661-016-3470-2.

[20] Y.S. Lee, P. Nandwana, W. Zhang, Dynamic simulation of powder packing structure for powder bed additive manufacturing, Int. J. Adv. Manuf. Technol. 96 (2018) 1507–1520. doi:10.1007/s00170-018-1697-3.

[21] M. Markl, C. Körner, Powder layer deposition algorithm for additive manufacturing simulations, Powder Technol. 330 (2018) 125–136. doi:10.1016/j.powtec.2018.02.026.

[22] A. Foroozmehr, M. Badrossamay, E. Foroozmehr, S. Golabi, Finite Element Simulation of Selective Laser Melting process considering Optical Penetration Depth of laser in powder bed, Mater. Des. 89 (2016) 255–263. doi:10.1016/j.matdes.2015.10.002.

[23] W. Nan, G. Mojtaba, Numerical simulation of powder flow during spreading in additive manufacturing, Powder Technol. 342 (2019) 801–807. doi:10.1016/j.powtec.2018.10.056.

[24] T.R. Society, B. Sciences, K.L. Johnson, K. Kendall, A.D. Roberts, Surface Energy and the Contact of Elastic Solids, Proc. R. Soc. London A Math. Phys. Eng. Sci. 324 (1971) 301–313. doi:10.1098/rspa.1971.0141.

[25] Y. Tsuji, T. Tanaka, T. Ishida, Lagrangian numerical simulation of plug flow of cohesionless particles in a horizontal pipe, Powder Technol. 71 (1992) 239–250. doi:10.1016/0032-5910(92)88030-L.

[26] H. SAKAGUCHI, E. OZAKI, T. IGARASHI, Plugging of the Flow of Granular Materials during the Discharge from a Silo, Int. J. Mod. Phys. B. (2004). doi:10.1142/s0217979293002705.

[27] T. Etter, K. Kunze, F. Geiger, H. Meidani, Reduction in mechanical anisotropy through high temperature heat treatment of Hastelloy X processed by Selective Laser Melting

(SLM), IOP Conf. Ser. Mater. Sci. Eng. 82 (2015) 012097. doi:10.1088/1757-899X/82/1/012097.

[28] Zhou Y.C., Y.C.Zhou, et al. Rolling friction in the dynamic simulation of sandpile formation.pdf, Phys. A Stat. Mech. Its Appl. (1999). doi:0378-4371/99.

[29] A. Castellanos, The relationship between attractive interparticle forces and bulk behaviour in dry and uncharged fine powders, Adv. Phys. (2005). doi:10.1080/17461390500402657.

[30] J. Visser, Van der Waals and other cohesive forces affecting powder fluidization, Powder Technol. (1989). doi:10.1016/0032-5910(89)80001-4.

[31] Standard Test Methods for Tension Testing of Metallic Materials, (n.d.). https://compass.astm.org/Standards/HISTORICAL/E8E8M-13A.htm (accessed September 15, 2018).

[32] Q. Han, R. Setchi, S.L. Evans, Synthesis and characterisation of advanced ball-milled Al-Al2O3 nanocomposites for selective laser melting, Powder Technol. 297 (2016) 183–192. doi:10.1016/j.powtec.2016.04.015.

[33] B. AlMangour, D. Grzesiak, J.M. Yang, In situ formation of TiC-particle-reinforced stainless steel matrix nanocomposites during ball milling: Feedstock powder preparation for selective laser melting at various energy densities, Powder Technol. 326 (2018) 467–478. doi:10.1016/j.powtec.2017.11.064.

[34] A. Simchi, Direct laser sintering of metal powders : Mechanism , kinetics and microstructural features, Mater. Sci. Eng. 428 (2006) 148–158. doi:10.1016/j.msea.2006.04.117.

[35] S.A. Khairallah, A.T. Anderson, A. Rubenchik, W.E. King, Laser powder-bed fusion additive manufacturing: Physics of complex melt flow and formation mechanisms of pores, spatter, and denudation zones, Acta Mater. 108 (2016) 36–45.

[36] W.E. King, H.D. Barth, V.M. Castillo, G.F. Gallegos, J.W. Gibbs, D.E. Hahn, C. Kamath, A.M. Rubenchik, Observation of keyhole-mode laser melting in laser powder-bed fusion additive manufacturing, J. Mater. Process. Technol. 214 (2014) 2915–2925. doi:10.1016/j.jmatprotec.2014.06.005.

[37] N.T. Aboulkhair, I. Maskery, C. Tuck, I. Ashcroft, N.M. Everitt, On the formation of AlSi10Mg single tracks and layers in selective laser melting: Microstructure and nano-mechanical properties, J. Mater. Process. Technol. 230 (2016) 88–98. doi:10.1016/j.jmatprotec.2015.11.016.